

See discussions, stats, and author profiles for this publication at: <https://www.researchgate.net/publication/275364944>

Balancing stability and specific energy in Li-rich cathodes for lithium ion batteries: A case study of a novel Li-Mn-Ni-Co oxide

ARTICLE · APRIL 2015

DOI: 10.1039/C5TA00929D

CITATIONS

2

READS

37

7 AUTHORS, INCLUDING:



Guangshe Li

Chinese Academy of Sciences

178 PUBLICATIONS 4,129 CITATIONS

SEE PROFILE



Chaochao Fu

Chinese Academy of Sciences

14 PUBLICATIONS 178 CITATIONS

SEE PROFILE



Jianming Fan

Chinese Academy of Sciences

7 PUBLICATIONS 64 CITATIONS

SEE PROFILE



Liping Li

Chinese Academy of Sciences

205 PUBLICATIONS 4,216 CITATIONS

SEE PROFILE

CrossMark
click for updates

Cite this: DOI: 10.1039/c5ta00929d

Balancing stability and specific energy in Li-rich cathodes for lithium ion batteries: a case study of a novel Li–Mn–Ni–Co oxide†

Qi Li, Guangshe Li, Chaochao Fu, Dong Luo, Jianming Fan, Dongjiu Xie and Liping Li*

Lithium batteries for UPS, portable electronics and electrical vehicles rely on high-energy cathodes. Li-rich manganese-rich oxide ($x\text{Li}_2\text{MnO}_3 \cdot (1-x)\text{LiMO}_2$, $M = \text{transition metals}$) is one of the few materials that might meet such a requirement, but it suffers from poor energy retention due to serious voltage and/or capacity fade, which challenges its applications. Here we show that this challenge can be addressed by optimizing the interactions between the components Li_2MnO_3 and LiMO_2 in the Li-rich oxide (*i.e.* stabilizing the layered structure through Li_2MnO_3 and controlling Li_2MnO_3 activation through LiMO_2). To realize this synergistic effect, a novel Li_2MnO_3 -stabilized $\text{Li}_{1.080}\text{Mn}_{0.503}\text{Ni}_{0.387}\text{Co}_{0.030}\text{O}_2$ was designed and prepared using a hierarchical carbonate precursor obtained by a solvo/hydro-thermal method. This layered oxide is demonstrated to have a high working voltage of 3.9 V and large specific energy of 805 W h kg^{-1} at 29°C as well as impressive energy retention of 92% over 100 cycles. Even when exposed to 55°C , energy retention is still as high as 85% at 200 mA g^{-1} . The attractive performance is most likely the consequence of the balanced stability and specific energy in the present material, which is promisingly applicable to other Li-rich oxide systems. This work sheds light on harnessing Li_2MnO_3 activation and furthermore efficient battery design simply through compositional tuning and temperature regulation.

Received 4th February 2015

Accepted 12th April 2015

DOI: 10.1039/c5ta00929d

www.rsc.org/MaterialsA

1. Introduction

The urgent need for high-energy batteries nowadays is self-evident. The criterion of specific energy (energy per unit mass) is usually utilized to quantify the energy density of a battery, which equals the integral area of the discharge profile, specifically, calculated from

$$\text{specific energy} = \int_0^Q V_d(q) dq$$

where Q is the maximum discharge capacity, q represents the state of charge of a cell and $V_d(q)$ is the corresponding discharge voltage. Therefore, specific energy is decided by the (1) discharge voltage and (2) discharge capacity, implying two strategies to increase the energy density of a cell, *i.e.* increasing the discharge voltage (evaluated by the average voltage) and/or enhancing the discharge capacity.

When compared to conventional battery systems, lithium ion batteries (LIBs) are known to be of high energy density because of the high working voltage and large discharge capacity.^{1–6} Since the practically achievable energy of the cathode is much

inferior to that of the anode, energy density of LIBs is largely determined by the cathode part. According to the definition given above, the specific energy is actually closely relevant to the shape of the discharge profile, and ultimately determined by the redox couples (*i.e.* composition-dependent). Until now, various cathodes of Li–Mn–Ni–Co oxides for LIBs have been developed for commercial use (Table S1†), among which the highest energy density of 685 W h kg^{-1} was obtained from $\text{LiNi}_{0.8}\text{Co}_{0.15}\text{Al}_{0.05}\text{O}_2$ (NCA) with the best-case 3.7 V working voltage and 185 mA h g^{-1} discharge capacity. However, energy density still needs to be improved to meet the increasing demand for power.

Structurally integrated Li-rich manganese-rich oxides, $x\text{Li}_2\text{MnO}_3 \cdot (1-x)\text{LiMO}_2$ ($M = \text{transition metals}$) with layered structures have attracted international attention and are being aggressively pursued as alternative high-capacity cathodes in LIBs.^{4,7} The most investigated series of Li-rich oxides $0.5\text{Li}_2\text{MnO}_3 \cdot 0.5\text{LiMn}_x\text{Ni}_y\text{Co}_z\text{O}_2$ ($x + y + z = 1$) deliver a capacity higher than 250 mA h g^{-1} at a working voltage of 3.6 V,^{8–18} seemingly to provide a much higher energy density even exceeding 1000 W h kg^{-1} . Unfortunately, this kind of material suffers serious voltage fade due to a notorious layered-to-spinel phase transformation during cycling.^{9,19–22} Sometimes this transformation process yields electrochemically active spinel variants, which may contribute to the discharge capacity, thus retaining its high capacity.¹⁹ Even so, the voltage fade would result in a very rapid degradation in energy density (Fig. S4†), thus hindering the applications. Many investigations intended to enhance the

Key Laboratory of Design and Assembly of Functional Nanostructures, Fujian Institute of Research on the Structure of Matter, Chinese Academy of Sciences, Fuzhou 350002, PR China. E-mail: lipingli@fjirsm.ac.cn

† Electronic supplementary information (ESI) available. See DOI: 10.1039/c5ta00929d

structural stability of $0.5\text{Li}_2\text{MnO}_3 \cdot 0.5\text{LiMn}_x\text{Ni}_y\text{Co}_z\text{O}_2$ ($x + y + z = 1$) through lattice modification^{9,10,21,23,24} or surface treatments.^{19,25,26} Progress has been achieved to some extent. Nevertheless, the thermodynamically favorable transformation during cycling is barely successfully countered,^{9,27} and the additional treatment procedures imposed are against one's best expectation for a cost-effective and time-saving production line of LIBs.

It is well documented that Li-rich layered oxides can be assigned to a "composite" structure between trigonal $R\bar{3}m$ (LiMO_2) and monoclinic $C2/m$ (Li_2MnO_3) crystal unit cells, which are intimately mixed over several nanometers scale.^{28–33} Note that LiMO_2 and Li_2MnO_3 structures have similar cubic closed-packed (ccp) layers with an interlayer spacing of 4.7 Å, (001) for layered monoclinic and (003) for layered trigonal.³⁴ This allows both structures to integrate perfectly and form a layered-layered integrated composite material. Distinctly different from conventional composite systems with macroscale inhomogeneity, the components LiMO_2 and Li_2MnO_3 for Li-rich composites are distributed in nano-domains/nano-crystals with mutual interactions. It is thus highly possible to achieve high-energy density without sacrificing the stability simply through modulating this "mutual interaction" by tailoring the Li_2MnO_3 content and/or tuning the composition of the end member LiMO_2 . To achieve this goal, it is necessary to understand the respective role of Li_2MnO_3 and LiMO_2 . On the one hand, Li_2MnO_3 plays an important part in stabilizing the layered structure of LiMO_2 : (i) the $\text{Li}_2\text{Mn}^{(\text{IV})}\text{O}_3$ component is electrochemically inactive below 4.4 V, since Mn^{4+} can hardly be oxidized further during charge. Moreover, no lithium ions can be inserted into the ideal Li_2MnO_3 structure during discharge as no energetically favorable interstitials are available. Therefore, Li_2MnO_3 could act as a stabilizer of the whole layered structure; (ii) during the charge process of the LiMO_2 component, depletion of lithium ions from the lithium layer could be compensated by the diffusion of lithium from octahedral sites in the manganese layer of the Li_2MnO_3 component to tetrahedral sites in the lithium-depleted layer, thereby reducing the concentration of tri-vacancies, the prerequisites for phase transition,^{27,35} and thus providing the additional binding energy necessary to maintain the structural stability of the ccp array during lithium extraction.^{4,36–38} On the other hand, LiMO_2 is essential in determining the rate and extent of Li_2MnO_3 activation. As it is well known that electrochemical activation of Li_2MnO_3 is accompanied by ion rearrangement as well as formation of oxygen vacancy, these processes are heavily dependent on the surrounding atomic distributions (*i.e.* the composition of the LiMO_2 component).^{7,23,39–43} Such an effect could be exerted through the interface of the above-mentioned nano-domains/nano-crystals, and evolves from surface to "bulk" atoms. Charge-carriers (*i.e.*, electrons and lithium ions) can relatively freely travel between both phases, which also facilitates interaction between Li_2MnO_3 and LiMO_2 . Therefore, it is tempting to speculate that battery cathodes of high specific energy and high stability can be achieved through proper compositional synergism of the Li–Mn–Ni–Co oxide (*e.g.* stabilizing the layered structure with the component Li_2MnO_3 and controlling the activation of the component Li_2MnO_3 with LiMO_2).

Herein, we show an example of compositional synergism in optimizing the interactions between components Li_2MnO_3 and LiMO_2 in a Li-rich manganese-based oxide. A novel composition of Li_2MnO_3 -stabilized Li–Mn–Ni–Co oxide $\text{Li}_{1.080}\text{Mn}_{0.503}\text{Ni}_{0.387}\text{Co}_{0.030}\text{O}_2$ of a layered structure was obtained using a hierarchical carbonate precursor obtained by a solvo/hydro-thermal method. This composition is demonstrated to show a high energy density and excellent stability at 29 °C. Strikingly, such excellent electrochemical performance was retained at a high temperature of 55 °C. The findings reported herein are highly useful to highlight the correlation among composition, test temperature and electrochemical processes of Li-rich composite materials using a two-component structural model, which also provide hints for exploring more lithium-rich high-energy and high-stability cathodes for advanced lithium-ion batteries of diverse applications.

2. Experimental section

2.1 Sample synthesis

The carbonate precursor was prepared through a facile solvo/hydro-thermal method. The preparation procedure can be briefly described as follows: 0.7843 g manganese acetate, 0.6470 g nickel acetate and 0.0498 g cobalt acetate were mixed with 0.7207 g urea in a Teflon-lined autoclave containing ultrapure water and ethanol as the solvent (volume ratio of water to ethanol was fixed at 2 : 1). The mixed solution sealed in the autoclave was reacted at 200 °C for 36 h. After cooling to room temperature, the obtained powder was filtered and washed with ethanol three times to obtain the green carbonate precursor.

To prepare the target layered oxide, stoichiometric lithium hydroxide was mixed with the obtained carbonate precursor, and thereafter the mixture was sintered at 900 °C for 12 h at a ramping rate of 4 °C min^{−1}.

Reference samples of lower-lithium-concentration oxide, $\text{Li}_{0.98}\text{Mn}_{0.503}\text{Ni}_{0.38}\text{Co}_{0.03}\text{O}_2$ (Fig. S8†), and 5-5 Li-rich oxide, $0.5\text{Li}_2\text{MnO}_3 \cdot 0.5\text{LiMn}_{1/3}\text{Co}_{1/3}\text{Ni}_{1/3}\text{O}_2$ (Fig. S4 and S13†), were also prepared using a similar preparation method.

2.2 Sample characterization

Powder X-ray diffraction (PXRD) was carried out on a Rigaku Miniflex apparatus using a Cu source ($\text{Cu K}\alpha$, $\lambda = 1.5418$ Å). The obtained data were calculated on a General Structure Analysis System (GSAS)⁴⁴ for structure refinement. Field-emission scanning electron microscopy (SEM) (JEOL, model JSM-6700) was used for morphology studies. Chemical compositions of the samples were analyzed by inductively coupled plasma atomic emission spectrometry (ICP-AES) with a relative error of $\pm 2\%$. Transmission electron microscope (TEM) observation was conducted on a JEOL, model JEM-2100. X-ray photoelectron spectroscopy (XPS) was recorded on an ESCA-LAB MKII apparatus performed with a monochromatic Al K α X-ray source. The charging shift was calibrated using the C 1s photoemission line at a binding energy of 284.8 eV.

2.3 Electrochemical tests

All electrochemical performances reported in this paper were evaluated with 2025 coin cells using a Neware Test System. Unless otherwise specified, all the tests as presented in this paper were carried out in the voltage range of 2.0–4.8 V. The cathode laminate was composed of layered oxide powder (80 wt%), carbon black (super P Li, 10 wt%) as the conductive agent, and polyvinylidene fluoride (PVDF, 10 wt%) as the binder. 1 M of LiPF_6 in a 1:1:1 volume ratio of EC : DMC : EMC solution was used as an electrolyte. A Celgard 2500 polypropylene separator and Li metal foil were used as the separator and counter electrode, respectively. Electrochemical impedance spectroscopy (EIS) and cyclic voltammogram measurements were carried out on an electrochemical workstation (CHI660C). In order to precisely control and monitor the test temperature, all the coin cells subjected to electrochemical tests were placed in an incubator (Hongdu, SHP-160) with a regulated temperature of 29 or 55 °C.

3. Results and discussion

3.1 Synthesis of spherical layered



Fig. 1a illustrates the preparation process of the layered oxide, $\text{Li}_{1.080}\text{Mn}_{0.503}\text{Ni}_{0.387}\text{Co}_{0.030}\text{O}_2$ (calculated from ICP-AES results), as elaborated in the Experimental section.

Morphological studies (Fig. S1†) indicate that a large-scale uniform spherical precursor was obtained through a solvo/hydro-thermal method. When scaling up, each individual sphere (Fig. 1b) is observed to be assembled by nanocubes (Fig. 1c). The formation of the nanocube-like morphology could be closely related to the co-existence of H_2O and ethanol in the solvo/hydro-thermal system, which will be reported later. Qualitative XRD data analyses of the spherical precursor reveal the coexistence of manganese and nickel carbonates with a clear distinction between the Bragg peaks, while cobalt carbonate is hardly observed due to its low content and peak overlapping with the above two primary constituents. After calcination at high temperatures, the spherical morphology was inherited from that of the precursor (Fig. 1d), while the crystalline phases were totally changed. The XRD pattern well resembles those reported in previous studies for two-phase integrated composites.^{29,33} As shown in Fig. 1f, XRD data for the calcined product could be indexed to a typical layered structure ($R\bar{3}m$), while the weak reflections between two theta of 20–25° are associated with Li/Mn ordering in the Li_2MnO_3 phase ($C2/m$). Based on the structural refinement analysis using a two-phase model on the GSAS program, the lattice parameters for both $R\bar{3}m$ and $C2/m$ phases are obtained and tabulated in Table 1. The $C2/m$ phase fraction is 20.6%, structurally integrated with the 79.4% $R\bar{3}m$ phase, thus forming a Li_2MnO_3 -stabilized layered oxide.

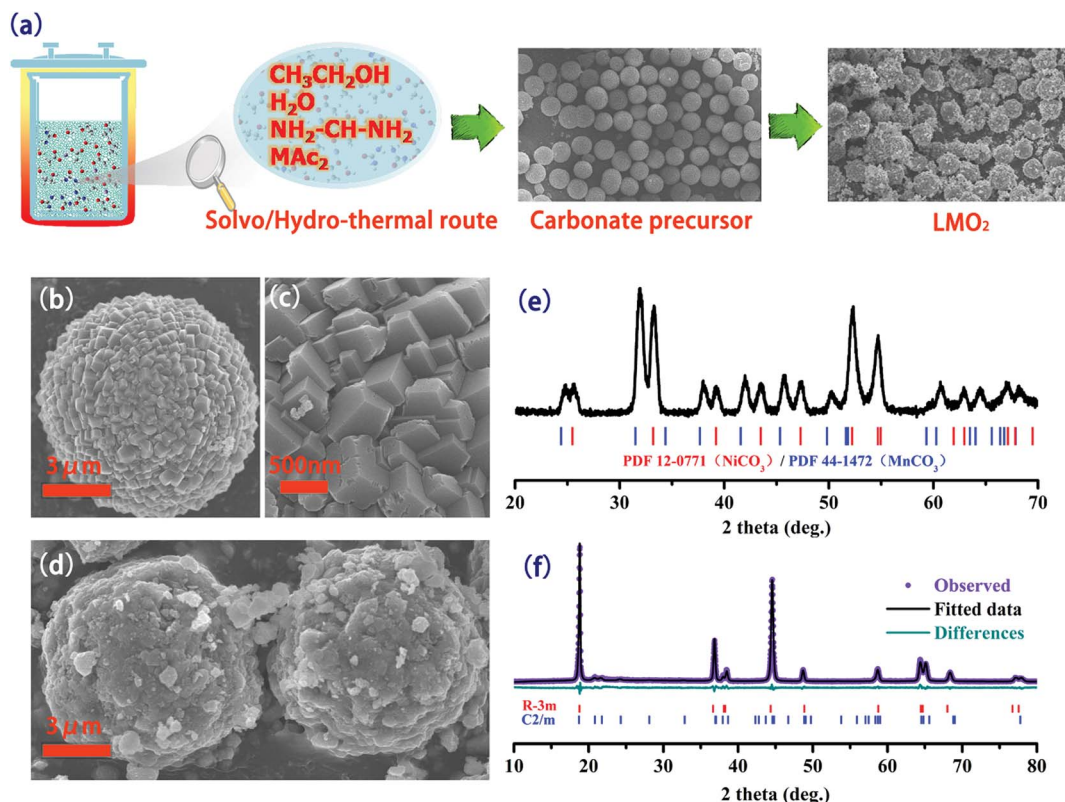


Fig. 1 (a) Synthesis route to the spherical carbonate precursor by the solvo/hydro-thermal method and the layered target oxide after a subsequent calcination; (b, c, e) SEM images and XRD pattern of the carbonate precursor; and (d, f) SEM images and XRD pattern for the layered oxide.

Table 1 Refined lattice parameters for $R\bar{3}m$ and $C2/m$ phases of the layered oxides

$R\bar{3}m$			$C2/m$				R_{wp}
a (Å)	b (Å)	Fraction ^a	a (Å)	b (Å)	c (Å)	Fraction ^a	
2.87021(7)	14.2660(8)	79.4%	5.01089(9)	8.612(1)	5.049(1)	20.6%	0.0683

^a Mole fraction.

In order to shed light on the local structure of the prepared oxide, we performed a high-resolution TEM observation on a random particle. As shown in Fig. 2a, for a limited area of *ca.* 30 nm \times 30 nm, the diffraction information is extracted using the Fast Fourier Transformation (FFT) pattern. The FFT pattern (inset of Fig. 2a) can be indexed as the diffractions along equivalent zone axes of $[12\bar{1}]_R$ in $R\bar{3}m$ (trigonal) and $[001]_M$ in $C2/m$ (monoclinic) phases. A simulated pattern is displayed in Fig. 2b, where the visible dots in the experimental pattern are highlighted by coloring. Basically, the FFT pattern seems to show strong trigonal diffractions (larger/blue dots), and the dots superimposed onto this pattern can be considered to correlate with $C2/m$ (monoclinic) phases (smaller/red ones). The detailed index of both phases is shown in Fig. 2c and d. Six highlighted dots in Fig. 2c represent the six brightest ones in the experimental pattern of Fig. 2a, and can be well indexed to planes of the $R\bar{3}m$ phase, as labeled in Fig. 2c. The hexagonal pattern highlighted in panel d is distinctive of $C2/m$ because the plane angle of 61.25° was detected between (110) with a d -spacing of 4.14 Å and (020) with an interplanar spacing of 4.31 Å. Note that partial $C2/m$ diffraction dots are superimposed with those of the $R\bar{3}m$ phase, *e.g.*, diffraction (130) marked by a square overlaps with the diffraction $(\bar{1}11)$ of $R\bar{3}m$. Overall, the abovementioned TEM data can be well interpreted by the assumption that $LiMO_2$ - and Li_2MnO_3 -like regions co-exist in the composite. A more detailed investigation of several

different local domains in this area is likely to suggest possible segregation of two regions in $Li_{1.080}Mn_{0.503}Ni_{0.387}Co_{0.030}O_2$ (Fig. S2†). Nevertheless, it should be pointed out that there exists debate on the real structure of Li-rich materials in the LIB research community. The $C2/m$ pattern as mentioned above is usually regarded as the result of cation ordering in the transition metal layer when taking Li-rich oxides as solid solutions. Yet further identification of atomic structures is demanding and beyond the scope of this study. Herein, of importance is that structural analyses including XRD and HR-TEM have clearly demonstrated the possibility of co-existence of Li_2MnO_3 - and $LiMO_2$ -like regions in our material. These proofs along with previous reports that evidenced Li-rich materials as two-phase structures^{28–33} underlie later discussions on electrochemistry.

Valence states of transition metal ions in $Li_{1.080}Mn_{0.503}Ni_{0.387}Co_{0.030}O_2$ were determined by XPS analysis (Fig. 3). The Mn 2p core-level spectrum shows two signals at *ca.* 642.6 and 654.1 eV, which are assigned to Mn 2p_{2/3} and Mn 2p_{1/2}, respectively. The spin-orbital splitting is *ca.* 11.5 eV, which indicates that manganese ions are present as Mn⁴⁺.^{45,46} This has been rationalized further by Mn 3s spectrum analysis, where two main peaks show a binding energy difference of 4.6 eV, consistent with literature reports on Mn⁴⁺ spectra.^{8,9,47} Concerning the valence states of Ni species in the samples, one can see core level photoelectron signals of Ni 2p_{2/3} at 854.5 eV, Ni

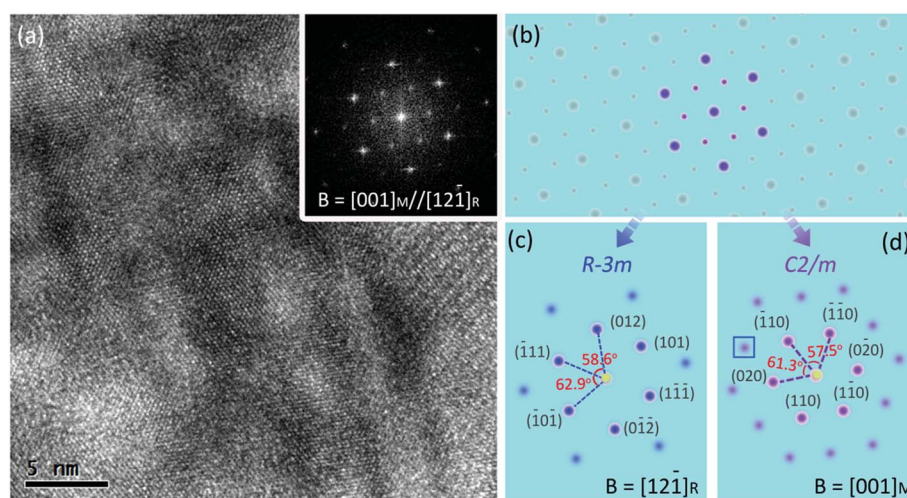


Fig. 2 Structural analysis of $Li_{1.08}Mn_{0.503}Ni_{0.387}Co_{0.03}O_2$: (a) HR-TEM image of a random particle and the average fast Fourier transformation (FFT) pattern; (b) simulated FFT pattern corresponding to experimental data in (a), which is an overlapping pattern of (c) the FFT pattern projected along $[12\bar{1}]_R$ for the $R\bar{3}m$ phase, and (d) the FFT pattern projected along $[001]_M$ for the $C2/m$ phase.

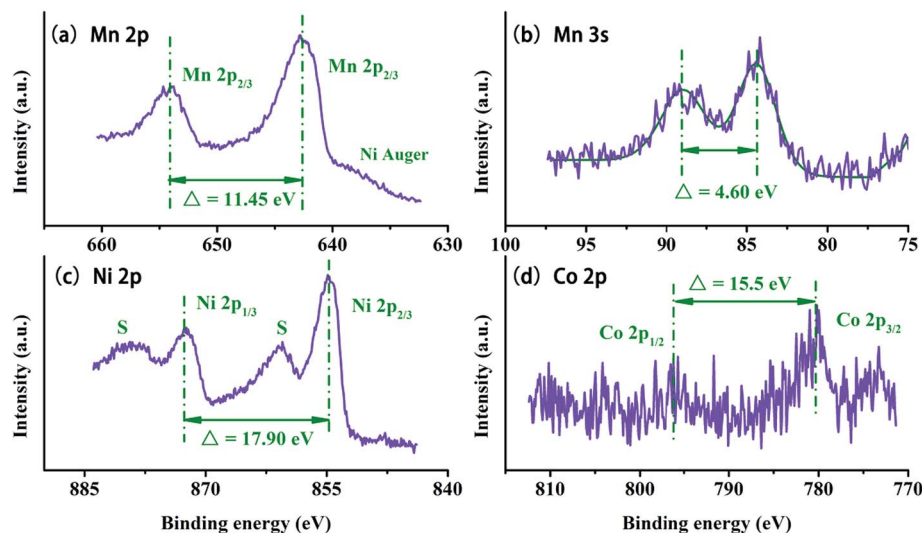


Fig. 3 XPS spectra of (a) Mn 2p, (b) Mn 3s, (c) Ni 2p and (d) Co 2p for the layered oxide after calcination.

$2p_{1/2}$ at 872.4 eV, and two satellite peaks (Fig. 3c). The spin-orbital splitting between Ni $2p_{2/3}$ and $2p_{1/3}$ is 17.9 eV, implying the existence of Ni^{2+} .^{48–50} In contrast to the intense core-level signals for Mn and Ni species, the core-level signal for Co 2p is weak in intensity due to its low content. Even so, the Co species can be affirmed as Co^{3+} in a low-spin state, suggested by two distinguishable signals at *ca.* 780.0 and 795.5 eV.^{48,50–52} These XPS results indicate that the metal elements of the prepared sample were present in their stable valance states, which could be beneficial for rendering decent electrochemical performance and stability.

In the following, we will fully evaluate the electrochemical performance and stability of the samples by conducting galvanostatic charge/discharge tests at 29 °C and 55 °C.

3.2 Electrochemical performance of spherical

$Li_{1.080}Mn_{0.503}Ni_{0.387}Co_{0.030}O_2$ at 29 °C

The initial charge profile (Fig. 4a) recorded at 29 °C displays a smooth ramp in the voltage range between 3.8 and 4.4 V along with a very limited plateau above 4.4 V. The smooth ramp is attributed to the oxidation of $Ni^{2+/3+/4+}$ and $Co^{3+/4+}$ from the dominant $LiMO_2$ -like ($R\bar{3}m$) phase,^{53,54} while the plateau region is supposed to reflect the electrochemical behavior of the Li_2MnO_3 -like region ($C2/m$) which is absent in the second charge process. Discharge profiles of the two selected cycles exhibited little difference. The corresponding dQ/dV data are plotted (Fig. 4b) to get a clear view of the different electrochemical behaviors. Obviously, in the first charge process, the peak intensity at 4.5 V is lower than that at *ca.* 3.9 V, which indicates the limited capacity contribution from the Li_2MnO_3 -like component at 29 °C. In the subsequent cycle, the low-potential peak shifted towards lower voltages (labeled as O1), and the peak at 4.5 V becomes invisible. Carefully examining the discharge branch of the dQ/dV plots, two major peaks are clearly observed: one at *ca.* 4.4 V (denoted as R2) was associated with Li occupation within tetrahedral sites coupled with O2

hump at a similar potential in the charge branch. Another one at *ca.* 3.8 V (denoted as R1) is ascribed to Li occupation within octahedral sites accompanied by $Ni^{4+/3+/2+}$ and $Co^{4+/3+}$ redox couples.^{9,13,55} The peak position of R1 is nearly coincident with that of O1, suggesting that the redox couple is highly reversible resulting in considerable cycling stability, which is confirmed by the cycling tests (Fig. 4c). The initial discharge capacity at 20 mA g^{-1} reached 211 mA h g^{-1} , which still remained as high as 206 mA h g^{-1} after 100 cycles (capacity retention = 98%). It is well documented that Li_2MnO_3 -containing oxide cathodes are confronted with a barrier that the voltage degrades during the cycling process, which seriously hinders their applications, because voltage fade would result in a dramatic decrease in energy density even though fading of discharge capacity could be prevented.^{19,21,56} For example, $Li_{1.2}Ni_{0.15}Co_{0.10}Mn_{0.55}O_2$ was coated with AlF_3 in order to upgrade its energy density retention, and capacity degradation was successfully countered while voltage fade was still significant (decreased by *ca.* 0.37 V over 100 cycles, 90% retention), though it has been evidently improved as compared to the uncoated sample (decreased by 0.43 V, 87% retention). A sample with a widely studied composition of $Li_{1.20}Mn_{0.54}Co_{0.13}Ni_{0.13}O_2$ was also prepared and its performance is shown in Fig. S4,† clearly demonstrating the unsatisfactory voltage/energy retention (85.1%/79.9%) over 65 cycles, albeit with decent capacity retention (92%). In contrast, the layered oxide $Li_{1.080}Mn_{0.503}Ni_{0.387}Co_{0.030}O_2$ (with *ca.* 20 mol% Li_2MnO_3 component) in the present work, with no additional treatments, exhibits both excellent average voltage and energy density retention in the voltage range of 2.0–4.8 V: the decrease of average voltage is only 0.2567 V after 100 cycles (3.60 V, equal to 93% of the initial voltage, 3.86 V); energy density retains *ca.* 92% of the initial value (805 W h kg^{-1}) after 100 cycles. When compared to several commercial cathode materials (Table S1 and Fig. S3†), the current layered oxide $Li_{1.080}Mn_{0.503}Ni_{0.387}Co_{0.030}O_2$ is rather competitive as a potential alternative cathode for LIBs within power density and environmental considerations.

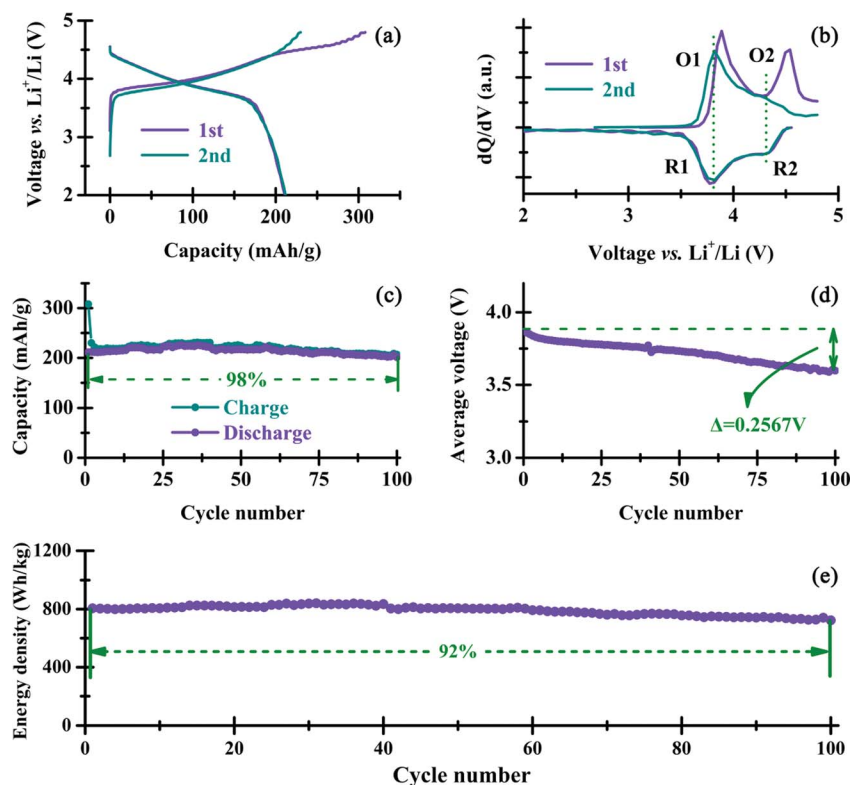


Fig. 4 Electrochemical performance of the spherical layered oxide measured at 29 °C at a rate of 20 mA g⁻¹ in the voltage range of 2.0–4.8 V: (a) initial and 2nd charge/discharge profiles; (b) dQ/dV profiles calculated from numerical data observed from the first two cycles; (c) charge/discharge capacity vs. cycle number; (d) normal average voltage vs. cycle number; and (e) specific energy density vs. cycle number.

In addition to the excellent energy density and superior voltage/capacity retention, the current layered material also delivers a reasonable rate capability at 29 °C. As shown in Fig. 5a, the initial discharge capacity values in the voltage range of 2.0–4.8 V at a rate of 20, 100, 200, 400, 600 and 1200 mA g⁻¹

are 210 (±1.4), 169 (±3.1), 162 (±3.3), 147 (±1.5), 145 (±3.3) and 126 (±2.8) mA h g⁻¹, respectively. From the corresponding cycling data in Fig. 5b, no dramatic capacity fading was seen after 200 cycles at all selected rates, suggesting a superior cycling stability.

In short, when used at 29 °C, the performance of the current layered oxide Li_{1.080}Mn_{0.503}Ni_{0.387}Co_{0.030}O₂ is quite attractive, especially for its excellent retention of working voltage and energy density.

3.3 Electrochemical performance of spherical Li_{1.080}Mn_{0.503}Ni_{0.387}Co_{0.030}O₂ at a high temperature of 55 °C

The layered oxide Li_{1.080}Mn_{0.503}Ni_{0.387}Co_{0.030}O₂ also exhibited rather considerable stability at a high temperature of 55 °C: capacity retentions at 200 and 400 mA g⁻¹ over 100 cycles are 91% and 86%, respectively (Fig. 6a). Under such harsh conditions of high temperature, the energy retentions are still as high as 85% at 200 mA g⁻¹ and 76% at 400 mA h g⁻¹.

To investigate the electrochemical behavior at a high temperature of 55 °C, the charge/discharge and dQ/dV profiles of the first two cycles are analyzed in Fig. 6b and c. Similar to Fig. 4b, O1–R1 and O2–R2 appear in the 2nd charge/discharge plot but become clearer and sharper. When compared with Fig. 4a and b, two major differences arising from increasing test temperature should be noted: (i) the plateau above 4.5 V is prolonged at 55 °C, resulting in a sharp peak at 4.5 V in the dQ/dV charge branch with its intensity surpassing that at 3.8 V; (ii)

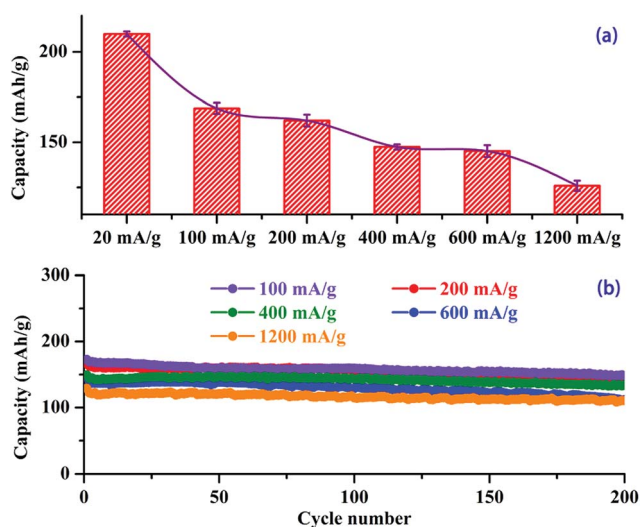


Fig. 5 Rate performance of the layered oxide Li_{1.080}Mn_{0.503}Ni_{0.387}Co_{0.030}O₂ in the voltage range of 2.0–4.8 V at 29 °C: (a) initial discharge capacity and (b) discharge capacity vs. cycle number at different current densities.

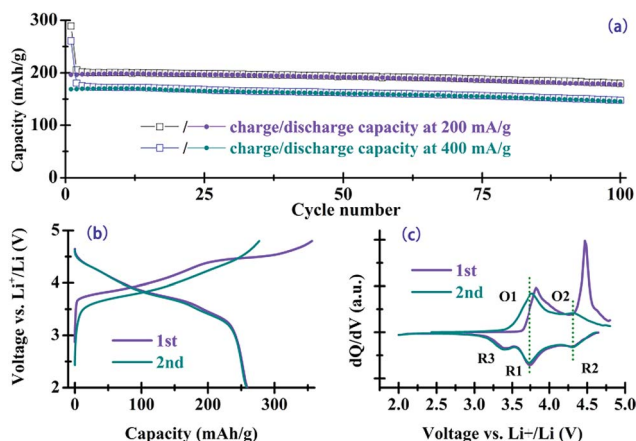


Fig. 6 Electrochemical performance of the layered oxides recorded in the voltage range of 2.0–4.8 V at 55 °C: (a) discharge capacity vs. cycle number at different current densities; (b) initial and 2nd charge/discharge profiles at 20 mA g⁻¹; (c) dQ/dV plot calculated from numeric data observed from (b).

in addition to the redox couples R1–O1 and R2–O2, a third reduction peak (denoted as R3) appears at *ca.* 3.3 V. These variations indicate different electrochemical behaviors of the current layered oxides at 29 °C and 55 °C, which motivate us to further investigate these temperature-dependent phenomena.

3.4 Differences in electrochemical behaviors and kinetics of spherical Li_{1.080}Mn_{0.503}Ni_{0.387}Co_{0.030}O₂ at 29 °C and 55 °C

Firstly, the initial two cyclic voltammograms at 29 °C and 55 °C were tested, as shown in Fig. 7a and b, respectively. The CV profiles show more similarity than differences with corresponding dQ/dV plots shown in Fig. 4b and 6c. This helps to confirm the observation recorded above, *i.e.* the appearance of the enhanced “Li₂MnO₃ peak” in the initial charge process and the new R3 peak in subsequent cycles when increasing the

testing temperature to 55 °C. These observations indicate that it is hard to activate the Li₂MnO₃-like component at 29 °C for the present layered oxide Li_{1.080}Mn_{0.503}Ni_{0.387}Co_{0.030}O₂. Increasing the temperature facilitates the activation process, and thus contributes more discharge capacity. The appearance of R3, as represented by the redox of Mn^{4+/3+},^{14,57} is consistent with the enhancement of the “Li₂MnO₃ peak” in the initial charge. In sharp contrast, the R3 peak is absent and the “Li₂MnO₃ peak” is rather weak in the CV curve at 29 °C, just proving its limited activation.

From CV curves in Fig. 7a, it is also found that peak positions of R1–O1 and O2–R2 showed a relatively larger mismatch, implying a larger polarization when tested at 29 °C under the CV testing conditions. On the other hand, no obvious difference between O1 and R1 is observed at 55 °C, and additionally peak O2 in the second cycle is much clear, demonstrating an enhanced kinetic property at high temperature.

The difference in kinetics is affirmed by further investigation by varying the scanning rate, as shown in Fig. 7c and d: increasing the scanning rate at 29 °C results in seriously distorted curves, with only two observable broad peaks in each loop. Comparatively, peaks of high-temperature CV curves in Fig. 7d are sharp and clearly distinguishable. Therefore, through the qualitative analysis by CV tests, one can notice that the electrode at 55 °C has a kinetic advantage over that at 29 °C.

EIS measurements shown in Fig. 7e and f give quantitative data about the kinetic differences at 29 °C and 55 °C. Both EIS data were fitted using an equivalent circuit in Fig. 7g, where *C*_{sl} and *C*_{dl} are the capacitances of SEI film and double layer, respectively; *W* is the Warburg impedance directly related to lithium ion diffusion. The total resistance *R*_{total} is the sum of *R*_e (internal resistance), *R*_{sf} (resistance of SEI film) and *R*_{ct} (bulk charge transfer resistance). The kinetic parameters thus obtained are listed in Table 2. *C*_{sl} and *C*_{dl} are found to be 10.03 μF and 6.71 mF at 29 °C, and 18.08 μF and 10.05 mF at 55 °C, respectively. It can be observed from Table 2 that charge

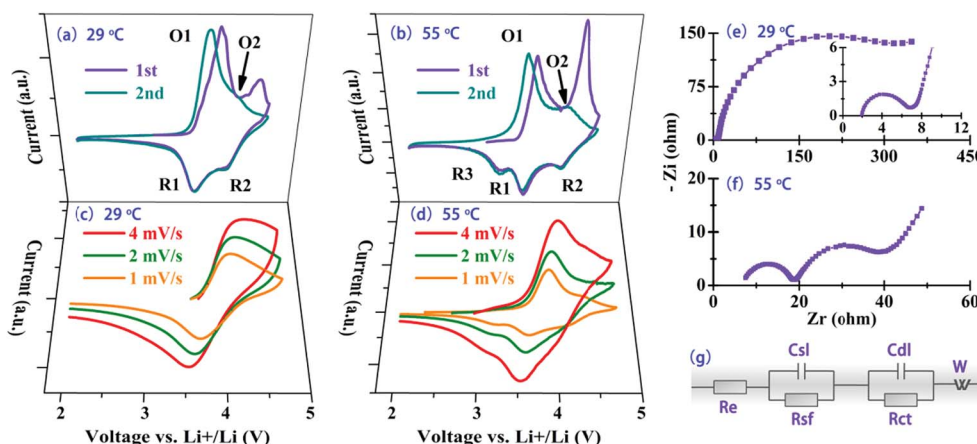


Fig. 7 Comparison of the electrochemical kinetics for layered oxides recorded at 29 °C and a high temperature of 55 °C. (a and b) First two cyclic voltammograms at a scan rate of 0.05 mV s⁻¹ in the voltage range of 2.0–4.8 V; (c and d) subsequent cyclic voltammograms at different scan rates; (e and f) EIS spectra at 4.6 V after the 1st cycle; and (g) equivalent circuit for EIS fitting.

Table 2 Kinetic parameters obtained at 29 °C and 55 °C for the layered oxides from equivalent circuit fitting of experimental EIS data

	R_c (ohm)	R_{sf} (ohm)	R_{ct} (ohm)	R_{total} (ohm)	$D(\text{Li}^+)$ ($\text{cm}^2 \text{s}^{-1}$)
29 °C	2.011 (± 0.08)	4.625 (± 0.16)	316.4 (± 18.03)	323.036	1.23×10^{-14}
55 °C	6.733 (± 0.11)	12.13 (± 0.16)	17.74 (± 0.32)	36.603	2.34×10^{-12}

transfer resistance is reduced dramatically from 316.4 to 17.74 ohm as temperature increases from 29 °C to 55 °C. Furthermore, the Warburg factor (σ) is estimated by linear fitting of Z_r vs. $\omega^{-1/2}$ ($0.01 \text{ Hz} < \omega < 0.1 \text{ Hz}$); thereafter the diffusion coefficient of lithium ions, $D(\text{Li}^+)$, can be calculated in terms of the equation, $D(\text{Li}^+) = 0.5R^2T^2/n^4A^2F^4C^2\sigma^2$.^{14,58} $D(\text{Li}^+)$ at 55 °C is calculated to be $2.34 \times 10^{-12} \text{ cm}^2 \text{s}^{-1}$, about two orders of magnitude higher than that at 29 °C ($1.23 \times 10^{-14} \text{ cm}^2 \text{s}^{-1}$). Therefore, high temperature is more favorable for the diffusion of lithium ions.

In brief, when cycling at 29 °C, the partial Li_2MnO_3 -like component in the spherical $\text{Li}_{1.080}\text{Mn}_{0.503}\text{Ni}_{0.387}\text{Co}_{0.030}\text{O}_2$ was activated (inadequate “plateau” chemistry). Correspondingly, only two redox couples contribute to the apparent capacity, and moreover, lithium ion diffusion is kinetically slow. When cycling at a high temperature of 55 °C, the activation of the Li_2MnO_3 -like component is enhanced (adequate “plateau” chemistry), resulting in an additional $\text{Mn}^{3+/4+}$ redox and more favored lithium ion diffusion.

3.5 Discussions of temperature-dependent electrochemical behavior of spherical $\text{Li}_{1.080}\text{Mn}_{0.503}\text{Ni}_{0.387}\text{Co}_{0.030}\text{O}_2$

Note that electrochemical activation of a layered cathode material is closely related to transition metal redox, lithium ion movements, and structural rearrangement. The diffusion pathways of lithium ions within the lattices along with charge/discharge processes have been intensively investigated.^{11,22,34,59–61} Herein we would like to offer a graphical illustration for this process based on a compositional phase diagram and corresponding initial charge/discharge profiles (Fig. 8).

Broadly speaking, a Li_2MnO_3 -integrated layered oxide locates on the Li_2MnO_3 – LiMO_2 tie-line. During the initial charge to ca. 4.4 V (charge – stage I), composition might change along the purple arrow until the Li_2MnO_3 – MO_2 tie-line is reached. Simultaneously, Ni^{2+} and Co^{3+} ions could be oxidized to the tetravalent state, which is accompanied by lithium extraction from the layered structure. When charged above 4.4 V (charge – stage II), the “inactive” Li_2MnO_3 component would be electrochemically activated, along with a rather complex structural rearrangement and oxygen loss. In this stage, the composition changes to the lithium-depleted layered MO_2 (ideal CdCl_2 -type) end member to complete the charge process (Fig. S7†). Thereafter, some lithium ions re-intercalate into MO_2 during the discharge process and finally reach the Li_2MnO_3 – LiMO_2 tie-line (ideally LiMO_2 apex), accompanied by concomitant Ni^{4+} and Co^{3+} reduction above 3.6 V and Mn^{4+} reduction below 3.6 V. These processes are illustrated in the charge/discharge plots of Fig. 8 (right part). A similar schematic of structural evolution can be found in ref. 62.

This phenomenon can be rationalized by correlating the electrochemical activation with the ion movement/rearrangement in the lattice. During the ionic movement/rearrangement processes, activation barrier plays a key role in determining the rate and degree. It is a common sense that the activation barrier of a migrating ion is controlled by its surrounding atoms (*i.e.* the composition), which has been widely supported by theoretical and experimental investigation.^{7,23,39,41,42,61,63} Therefore, it is deduced that for the specific composition of $\text{Li}_{1.080}\text{Mn}_{0.503}\text{Ni}_{0.387}\text{Co}_{0.030}\text{O}_2$, during stage II, the diffusion of Li ions from the transition-metal layers to Li layers as well as oxygen vacancy formation has a large activation barrier at 29 °C, resulting in inadequate Li_2MnO_3

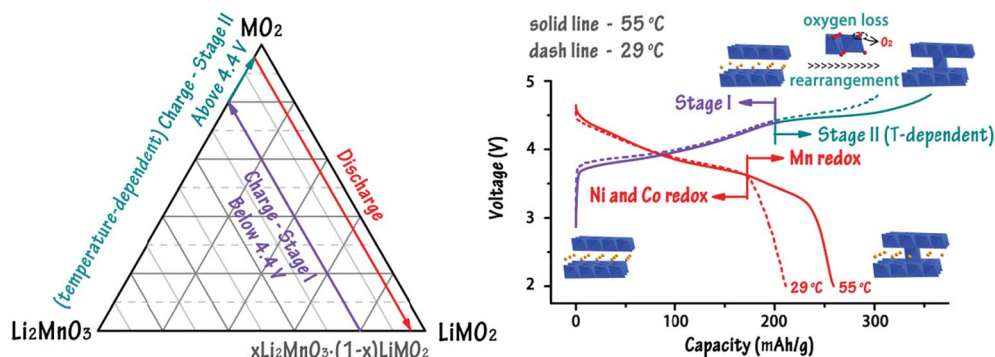


Fig. 8 Compositional phase diagram that shows the electrochemical reaction pathways for a $x\text{Li}_2\text{MnO}_3 \cdot (1-x)\text{LiMO}_2$ electrode (left) and the comparison of initial charge/discharge profiles obtained at 29 °C (dashed line) and a high temperature of 55 °C (solid line) with general schematic structure evolution⁶² (right).

activation. Therefore, the electrochemical characteristics of $\text{Li}_{1.08}\text{Mn}_{0.503}\text{Ni}_{0.387}\text{Co}_{0.03}\text{O}_2$ at 29 °C mainly originate from the layered component (LiMO_2). These results have been supported by the study regarding the temperature-dependent Li_2MnO_3 activation, in which Li_2MnO_3 activation is shown to be controlled by compositional tailoring and temperature regulation (Fig. S6†). Inadequate activation of Li_2MnO_3 -like regions at 29 °C could be advantageous in stabilizing the layered structure: during the charge process in stage I, depletion of lithium ions from the lithium layer of LiMO_2 is compensated by the diffusion of lithium from octahedral sites in the manganese layer of the Li_2MnO_3 component to tetrahedral sites in the lithium-depleted layer, thereby providing additional binding energy necessary to maintain structural stability.^{4,36,37} This allows capacity increase through raising the upper cut-off voltage with little sacrifice of cycling stability (Fig. S8†). In contrast, lowering the Li_2MnO_3 content results in compromised capacity retention in the voltage range of 2.0–4.8 V (Fig. S9†).

Additionally, layered-to-spinel conversion in Li-rich oxides is largely triggered by initial “ Li_2MnO_3 activation” (*i.e.*, “plateau” process), as reported elsewhere.⁶⁴ This sheds light on mitigating phase transformation and voltage fade by harnessing activation chemistry through modulating test conditions. A supplementary experiment well supports this hypothesis for $\text{Li}_{1.080}\text{Mn}_{0.503}\text{Ni}_{0.387}\text{Co}_{0.030}\text{O}_2$ (Fig. S10–S12†). Very recently, Wu *et al.* employed the HAADF-STEM technique to give direct evidence for this phenomenon. They investigated the surface structures of $\text{Li}_{1.2}\text{Mn}_{0.54}\text{Ni}_{0.13}\text{Co}_{0.13}\text{O}_2$ that were cycled at different voltage ranges, *i.e.* 2–4.4 V and 2–4.8 V, and found that when subject to low upper cut-off voltage (equals to less Li_2MnO_3 activation), Li-rich oxide suffered from a marginal layered-to-spinel transformation.⁵⁶ Therefore, it is tempting to unravel the excellent voltage retention over cycling at 29 °C in the present work by the explanation that layered-to-spinel transformation is rather limited due to the inadequate activation at 29 °C. The high stability of the layered composite

structure is confirmed by *ex situ* XRD measurements (Fig. 9): after 50 cycles at 29 °C, there still exist clear characteristic diffractions for the layered composite (Fig. 9, middle panel), with no impurities like the spinel variant as reported for many other Li-rich cathodes.^{10,20} Similarly, no impurities were observed after 50 cycles at 55 °C (Fig. 9, top panel), except that the main Bragg peaks became slightly broadened. Further XPS measurements of the corresponding laminates were conducted to test the possibility of valence state changes during cyclings. Owing to the influences from the binder, carbon additive, and surface layers as well, Mn 2p and Ni 2p spectra of the laminate sample displayed low intensity, but it still can be quantitatively seen that Mn and Ni species mainly maintained the oxidation states of 4+ and 2+, because peak centers of Mn 2p and Ni 2p are essentially unaltered relative to the pristine sample. This supplementary evidence is helpful for understanding the structural stability for the Li_2MnO_3 -integrated layered oxide, *i.e.* the presence of Mn^{4+} spectator ions keeps the average Mn oxidation state above 3+, thereby countering the effect of Jahn–Teller active Mn^{3+} (d4) ions that may destabilize manganese-oxide structures.^{7,65,66}

One has to note that in the LIB research community, lithium-rich materials could be regarded as homogeneous single-phase solid solution of the end members, Li_2MnO_3 and LiMO_2 , as advocated by some researchers.^{67–72} Therefore, the electrochemistry revealed here might be interpreted from different scenarios. The relevant discussion based on a composite structural model provides a graphical and straightaway comprehension into the electrochemistry of this class of materials, which could be instructive to explore Li-rich materials for various applications. We believe that the understanding from the composite structural model as well as the use of the compositional diagram makes it easy to follow the changes in the overall composition of the electrode during charging and discharging processes, thereby facilitating the balance of stability and specific energy in Li-rich cathodes for lithium ion batteries.

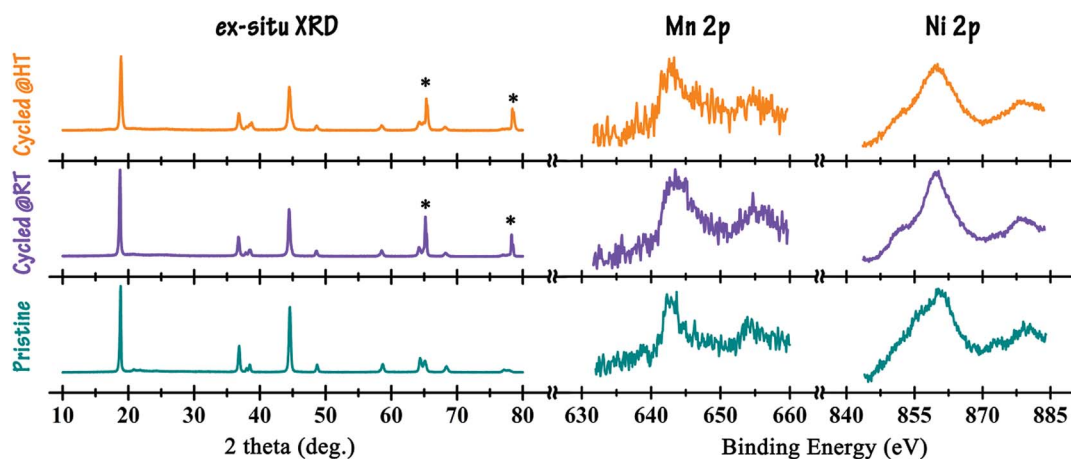


Fig. 9 *Ex situ* XRD pattern of pristine powder (bottom panel) and cycled laminates which were retrieved after 50 cycles at 200 mA g^{−1} at 29 °C (middle panel) and 55 °C (top panel), respectively, and corresponding Mn 2p and Ni 2p spectra. The symbol * represents the Bragg peaks of the Al current collector.

4. Conclusions

A novel high-performance layered oxide $\text{Li}_{1.080}\text{Mn}_{0.503}\text{Ni}_{0.387}\text{Co}_{0.030}\text{O}_2$ merited by balanced stability and specific energy was successfully prepared using a hierarchical carbonate as the precursor. At 29 °C, this layered oxide delivered a relatively high specific energy density of 805 W h kg⁻¹ as represented by a high working voltage of 3.9 V with an initial discharge capacity of 211 mA h g⁻¹ at 20 mA g⁻¹ and an energy density retention as high as 92% over 100 cycles. The cycling stability was superior over 200 cycles when charging/discharging at higher rates. Encouragingly, the electrochemical stability of this layered oxide can be retained even at a high temperature of 55 °C by showing a capacity retention of 91% at 200 mA g⁻¹ and 86% at 400 mA g⁻¹ over 100 cycles. The kinetic property is enhanced simultaneously. The high specific energy density and excellent stability of the $\text{Li}_{1.08}\text{Mn}_{0.506}\text{Ni}_{0.387}\text{Co}_{0.03}\text{O}_2$ layered oxide, outperforming practically achievable performances of state-of-the-art commercial cathodes, highlight its potential applications in high-energy lithium-ion batteries, particularly in backup batteries (e.g. the mobile power pack) and/or high-temperature batteries used for some specific applications. In addition, for the current layered oxide $\text{Li}_{1.080}\text{Mn}_{0.503}\text{Ni}_{0.387}\text{Co}_{0.030}\text{O}_2$, the layered LiMO_2 -like component is not sensitive to temperature, whereas the activation of the Li_2MnO_3 -like component is highly temperature-dependent, which well interprets the temperature-dependent electrochemical behavior observed. All these shed lights on a straightaway understanding into the electrochemistry of Li-rich materials, and further provide clues for efficient battery design by controlling Li_2MnO_3 activation ("plateau" chemistry) through compositional tailoring and temperature regulation, to reach the required performance standard.

Acknowledgements

This work was financially supported by NSFC (21271171 and 21025104) and the National Basic Research Program of China (2011CB935904).

Notes and references

- 1 J. B. Goodenough, *Energy Environ. Sci.*, 2014, 7, 14.
- 2 J.-M. Tarascon and M. Armand, *Nature*, 2001, **414**, 359–367.
- 3 J. R. Croy, A. Abouimrane and Z. Zhang, *MRS Bull.*, 2014, **39**, 407–415.
- 4 M. M. Thackeray, S.-H. Kang, C. S. Johnson, J. T. Vaughey, R. Benedek and S. A. Hackney, *J. Mater. Chem.*, 2007, **17**, 3112–3125.
- 5 M. M. Thackeray, C. Wolverton and E. D. Isaacs, *Energy Environ. Sci.*, 2012, **5**, 7854–7863.
- 6 J. Lee, A. Urban, X. Li, D. Su, G. Hautier and G. Ceder, *Science*, 2014, **343**, 519–522.
- 7 D. Kim, J. R. Croy and M. M. Thackeray, *Electrochem. Commun.*, 2013, **36**, 103–106.
- 8 C. Fu, G. Li, D. Luo, J. Zheng and L. Li, *J. Mater. Chem. A*, 2014, **2**, 1471–1483.
- 9 Q. Li, G. Li, C. Fu, D. Luo, J. Fan and L. Li, *ACS Appl. Mater. Interfaces*, 2014, **6**, 10330–10341.
- 10 W. He, D. Yuan, J. Qian, X. Ai, H. Yang and Y. Cao, *J. Mater. Chem. A*, 2013, **1**, 11397–11403.
- 11 C. H. Shen, L. Huang, Z. Lin, S. Y. Shen, Q. Wang, H. Su, F. Fu and X. M. Zheng, *ACS Appl. Mater. Interfaces*, 2014, **6**, 13271–13279.
- 12 S. J. Shi, J. P. Tu, Y. Y. Tang, Y. Q. Zhang, X. L. Wang and C. D. Gu, *J. Power Sources*, 2013, **240**, 140–148.
- 13 B. Song, H. Liu, Z. Liu, P. Xiao, M. O. Lai and L. Lu, *Sci. Rep.*, 2013, **3**, 3094.
- 14 B. Song, M. O. Lai and L. Lu, *Electrochim. Acta*, 2012, **80**, 187–195.
- 15 S. Guo, H. Yu, P. Liu, X. Liu, D. Li, M. Chen, M. Ishida and H. Zhou, *J. Mater. Chem. A*, 2014, **2**, 4422–4428.
- 16 Q. Xue, J. Li, G. Xu, H. Zhou, X. Wang and F. Kang, *J. Mater. Chem. A*, 2014, **2**, 18613–18623.
- 17 J. M. Zheng, Z. R. Zhang, X. B. Wu, Z. X. Dong, Z. Zhu and Y. Yang, *J. Electrochem. Soc.*, 2008, **155**, A775–A782.
- 18 Q. Li, G. Li, C. Fu, D. Luo, J. Fan, J. Zheng, D. Xie and L. Li, *Electrochim. Acta*, 2015, **154**, 249–258.
- 19 J. Zheng, M. Gu, J. Xiao, B. J. Polzin, P. Yan, X. Chen, C. Wang and J.-G. Zhang, *Chem. Mater.*, 2014, **26**, 6320–6327.
- 20 M. N. Ates, Q. Y. Jia, A. Shah, A. Busnaina, S. Mukerjee and K. M. Abraham, *J. Electrochem. Soc.*, 2014, **161**, A290–A301.
- 21 B. Song, C. Zhou, H. Wang, H. Liu, Z. Liu, M. O. Lai and L. Lu, *J. Electrochem. Soc.*, 2014, **161**, A1723–A1730.
- 22 D. Mohanty, J. Li, D. P. Abraham, A. Huq, E. A. Payzant, I. Wood, D. Lee and C. Daniel, *Chem. Mater.*, 2014, **26**, 6272–6280.
- 23 E.-S. Lee and A. Manthiram, *J. Mater. Chem. A*, 2014, **2**, 3932–3939.
- 24 M. Iftekhhar, N. E. Drewett, A. R. Armstrong, D. Hesp, F. Braga, S. Ahmed and L. J. Hardwick, *J. Electrochem. Soc.*, 2014, **161**, A2109–A2116.
- 25 X. Feng, Z. Yang, D. Tang, Q. Kong, L. Gu, Z. Wang and L. Chen, *Phys. Chem. Chem. Phys.*, 2014, **17**, 1257–1264.
- 26 J. R. Croy, D. Kim, M. Balasubramanian, K. Gallagher, S.-H. Kang and M. M. Thackeray, *J. Electrochem. Soc.*, 2012, **159**, A781–A790.
- 27 A. Vander Ven and G. Ceder, in *Lithium Batteries: Science and Technology*, ed. G. A. Nazri and G. Pistoia, Springer, New York, 2009, ch. 2, pp. 42–84.
- 28 J. Bareño, M. Balasubramanian, S. H. Kang, J. G. Wen, C. H. Lei, S. V. Pol, I. Petrov and D. P. Abraham, *Chem. Mater.*, 2011, **23**, 2039–2050.
- 29 D. Mohanty, A. Huq, E. A. Payzant, A. S. Sefat, J. Li, D. P. Abraham, D. L. Wood and C. Daniel, *Chem. Mater.*, 2013, **25**, 4064–4070.
- 30 D. Mohanty, A. S. Sefat, J. Li, R. A. Meisner, A. J. Rondinone, E. A. Payzant, D. P. Abraham, D. L. Wood IIIrd and C. Daniel, *Phys. Chem. Chem. Phys.*, 2013, **15**, 19496–19509.
- 31 H. Yu, R. Ishikawa, Y. G. So, N. Shibata, T. Kudo, H. Zhou and Y. Ikuhara, *Angew. Chem., Int. Ed. Engl.*, 2013, **52**, 5969–5973.
- 32 B. R. Long, J. R. Croy, F. Dogan, M. R. Suchomel, B. Key, J. G. Wen, D. J. Miller, M. M. Thackeray and M. Balasubramanian, *Chem. Mater.*, 2014, **26**, 3565–3572.

- 33 J. Rana, R. Kloepsch, J. Li, T. Scherb, G. Schumacher, M. Winter and J. Banhart, *J. Mater. Chem. A*, 2014, **2**, 9099–9110.
- 34 D. Mohanty, A. S. Sefat, S. Kalnaus, J. Li, R. A. Meisner, E. A. Payzant, D. P. Abraham, D. L. Wood and C. Daniel, *J. Mater. Chem. A*, 2013, **1**, 6249–6261.
- 35 J. Reed, G. Ceder and A. Van Der Ven, *Electrochem. Solid-State Lett.*, 2001, **4**, A78–A81.
- 36 C. P. Grey, W.-S. Yoon, J. Reed and G. Ceder, *Electrochem. Solid-State Lett.*, 2004, **7**, A290–A293.
- 37 K. Kang and G. Ceder, *Phys. Rev. B: Condens. Matter Mater. Phys.*, 2006, **74**, 091105.
- 38 M. M. Thackeray, C. S. Johnson, J. T. Vaughey, N. Li and S. A. Hackney, *J. Mater. Chem.*, 2005, **15**, 2257–2267.
- 39 D. Ye, C. Sun, Y. Chen, K. Ozawa, D. Hulicova-Jurcakova, J. Zou and L. Wang, *Nano Res.*, 2015, **8**, 808–820.
- 40 Y. Meng, G. Ceder, C. Grey, W.-S. Yoon, M. Jiang, J. Breger and Y. Shao-Horn, *Chem. Mater.*, 2005, **17**, 2386–2394.
- 41 M. Gu, I. Belharouak, A. Genc, Z. Wang, D. Wang, K. Amine, F. Gao, G. Zhou, S. Thevuthasan, D. R. Baer, J. G. Zhang, N. D. Browning, J. Liu and C. Wang, *Nano Lett.*, 2012, **12**, 5186–5191.
- 42 R. Xiao, H. Li and L. Chen, *Chem. Mater.*, 2012, **24**, 4242–4251.
- 43 D. Ye, B. Wang, Y. Chen, G. Han, Z. Zhang, D. Jurcakova, J. Zou and L. Wang, *J. Mater. Chem. A*, 2014, **2**, 18767–18774.
- 44 B. H. Toby, *J. Appl. Crystallogr.*, 2001, **34**, 210–213.
- 45 C. Yu, G. S. Li, X. F. Guan, J. Zheng and L. P. Li, *J. Alloys Compd.*, 2012, **528**, 121–125.
- 46 B. Song, Z. Liu, M. O. Lai and L. Lu, *Phys. Chem. Chem. Phys.*, 2012, **14**, 12875–12883.
- 47 S. Ardizzone, C. Bianchi and D. Tirelli, *Colloids Surf., A*, 1998, **134**, 305–312.
- 48 X. Zhang, D. Luo, G. Li, J. Zheng, C. Yu, X. Guan, C. Fu, X. Huang and L. Li, *J. Mater. Chem. A*, 2013, **1**, 9721–9729.
- 49 C. Fu, G. Li, D. Luo, Q. Li, J. Fan and L. Li, *ACS Appl. Mater. Interfaces*, 2014, **6**, 15822–15831.
- 50 G. Cherkashinin, D. Enslin and W. Jaegermann, *J. Mater. Chem. A*, 2014, **2**, 3571–3580.
- 51 F. Munakata, H. Takahashi, Y. Akimune, Y. Shichi, M. Tanimura, Y. Inoue, R. Itti and Y. Koyama, *Phys. Rev. B: Condens. Matter Mater. Phys.*, 1997, **56**, 979–982.
- 52 D. Luo, G. S. Li, C. Yu, L. S. Yang, J. Zheng, X. F. Guan and L. P. Li, *J. Mater. Chem.*, 2012, **22**, 22233–22241.
- 53 C. Wu, X. Fang, X. Guo, Y. Mao, J. Ma, C. Zhao, Z. Wang and L. Chen, *J. Power Sources*, 2013, **231**, 44–49.
- 54 H. J. Yu, H. J. Kim, Y. R. Wang, P. He, D. Asakura, Y. Nakamura and H. S. Zhou, *Phys. Chem. Chem. Phys.*, 2012, **14**, 6584–6595.
- 55 D. Kim, S.-H. Kang, M. Balasubramanian and C. S. Johnson, *Electrochem. Commun.*, 2010, **12**, 1618–1621.
- 56 Y. Wu, C. Ma, J. Yang, Z. Li, C. Liang, L. F. Allard and M. Chi, *J. Mater. Chem. A*, 2015, **3**, 5385–5391.
- 57 S. H. Kang, P. Kempgens, S. Greenbaum, A. J. Kropf, K. Amine and M. M. Thackeray, *J. Mater. Chem.*, 2007, **17**, 2069–2077.
- 58 D. Luo, G. Li, C. Fu, J. Zheng, J. Fan, Q. Li and L. Li, *Adv. Energy Mater.*, 2014, **4**, 1400062.
- 59 C. H. Shen, Q. Wang, F. Fu, L. Huang, Z. Lin, S. Y. Shen, H. Su, X. M. Zheng, B. B. Xu, J. T. Li and S. G. Sun, *ACS Appl. Mater. Interfaces*, 2014, **6**, 5516–5524.
- 60 D. Mohanty, S. Kalnaus, R. A. Meisner, K. J. Rhodes, J. L. Li, E. A. Payzant, D. L. Wood and C. Daniel, *J. Power Sources*, 2013, **229**, 239–248.
- 61 B. Xu, C. R. Fell, M. Chi and Y. S. Meng, *Energy Environ. Sci.*, 2011, **4**, 2223–2233.
- 62 N. Yabuuchi, K. Yoshii, S. T. Myung, I. Nakai and S. Komaba, *J. Am. Chem. Soc.*, 2011, **133**, 4404–4419.
- 63 R. Wang, X. He, L. He, F. Wang, R. Xiao, L. Gu, H. Li and L. Chen, *Adv. Energy Mater.*, 2013, **3**, 1358–1367.
- 64 Y. Kan, Y. Hu, C.-K. Lin, Y. Ren, Y.-K. Sun, K. Amine and Z. Chen, *Phys. Chem. Chem. Phys.*, 2014, **16**, 20697–20702.
- 65 J. Zheng, M. Gu, A. Genc, J. Xiao, P. Xu, X. Chen, Z. Zhu, W. Zhao, L. Pullan, C. Wang and J. G. Zhang, *Nano Lett.*, 2014, **14**, 2628–2635.
- 66 D. Kim, G. Sandi, J. R. Croy, K. G. Gallagher, S. H. Kang, E. Lee, M. D. Slater, C. S. Johnson and M. M. Thackeray, *J. Electrochem. Soc.*, 2013, **160**, A31–A38.
- 67 K. A. Jarvis, Z. Deng, L. F. Allard, A. Manthiram and P. J. Ferreira, *Chem. Mater.*, 2011, **23**, 3614–3621.
- 68 H. Koga, L. Croguennec, P. Mannesiez, M. Menetrier, F. Weill, L. Bourgeois, M. Duttine, E. Suard and C. Delmas, *J. Phys. Chem. C*, 2012, **116**, 13497–13506.
- 69 C. Genevois, H. Koga, L. Croguennec, M. Ménétrier, C. Delmas and F. Weill, *J. Phys. Chem. C*, 2015, **119**, 75–83.
- 70 H. Koga, L. Croguennec, M. Menetrier, P. Mannesiez, F. Weill and C. Delmas, *J. Power Sources*, 2013, **236**, 250–258.
- 71 H. Koga, L. Croguennec, M. Menetrier, K. Douhil, S. Belin, L. Bourgeois, E. Suard, F. Weill and C. Delmas, *J. Electrochem. Soc.*, 2013, **160**, A786–A792.
- 72 N. Tran, L. Croguennec, M. Ménétrier, F. Weill, P. Biensan, C. Jordy and C. Delmas, *Chem. Mater.*, 2008, **20**, 4815–4825.